

Two-line atomic fluorescence thermometry in the saturation regime

A. Manteghi · Y. Shoshin · N. J. Dam · L. P. H. de Goey

Received: 7 July 2014 / Accepted: 12 December 2014 / Published online: 30 December 2014
© Springer-Verlag Berlin Heidelberg 2014

Abstract Two-line atomic fluorescence (TLAF) thermometry is based on the consecutive excitation of two nearby atomic ground states to a common excited state, and ratioing the ensuing fluorescence yields. TLAF is one of the few methods that hold promise for thermometry in sooting environments. We extend the method to the regime of fully saturated excitation and introduce a new seeding system that also allows the method to be used in lean flames. We compare results for saturated TLAF to those of linear TLAF and to thermocouple measurements, and find good correspondence. The saturated version introduced here maximizes fluorescence yields while simultaneously suppressing the dependence on excitation laser irradiance.

1 Introduction

The development and optimization of combustion devices has been the subject of numerous studies in recent years. Different approaches have been employed to improve their performance in relation to achieving sustainable usage of non-renewable fossil energy sources, or to reduce the emission of pollutants such as NO_x , SO_x or soot particles which are potentially harmful for human health [1]. Combustion is a complex process in which several phenomena like chemical reactions, fluid dynamics, heat and mass transfer all interact with each other. These phenomena need to be known in detail to achieve a deeper understanding of the entire

process. Apart from chemical species concentration maps, temperature measurement in combusting media is of crucial importance because of the central role of temperature in determining reaction rates. Among the various thermometry techniques, optical methods have drawn a lot of attention because of their non-intrusive properties and because they in principle provide accurate information involving temporal and spatial distributions [2]. However, implementation of laser-based optical techniques in combustion is not trivial. Especially in strongly sooting media, the strong absorption, scattering, and spectral interference from other species are all reflected in the measured signal and complicate the analysis. In all of the laser diagnostics and optical thermometry methods for turbulent flames, the crucial parameters are accuracy, spatial resolution and the ability to measure on a short time scale. Two-line atomic fluorescence (TLAF) is one of the few techniques that meet these requirements and is also suitable for use in sooting environments [3, 4]. By using atoms rather than molecules, the electronic transition strength is not diluted over large numbers of rovibrational transitions, which considerably increases detection efficiency. By forming the excitation laser beam into a sheet, the temperature distribution can be imaged with an acceptable spatial resolution and by employing two cameras to capture sequentially two fluorescence images on a time scale that is short relative to the characteristic time scales of the combustion, say in less than 100 ns, the process is essentially frozen in time. Moreover, the temperature uncertainty of the TLAF method is potentially better than 100 K [5], making it suitable for temperature estimation in flames. Normally, suitable metal atoms (we focus on Indium (In) in this paper) are seeded into the flame, but using naturally occurring small molecular species like OH [6] and NO [7] has also been reported. From an experimental point of view, atoms are preferable due to higher oscillator strengths and simple spectra. The large

A. Manteghi · Y. Shoshin · N. J. Dam (✉) · L. P. H. de Goey
Combustion Technology, Eindhoven University of Technology,
PO Box 513, 5600 MB Eindhoven, The Netherlands
e-mail: N.J.Dam@tue.nl

A. Manteghi
e-mail: atieh.manteghi@gmail.com

spin-orbit splitting in the ground state of some metal atoms makes them well suited as target species in TLAF thermometry. Of course, such atoms are not native to the flame and must in some way be added. Typically, atoms like Indium are seeded into flames as InCl₃-salt dissolved in distilled water by using a nebulizer. Reported seeding concentrations vary from 4.5×10^{-4} to 1.0×10^{-2} mol/L with a seeding rate of 2.5 ml/h [8]. Adding the water seeding can decrease the flame temperature by just a few tens of degrees [9] to as much as 100–150 K (depends on the seeding system) and changes the soot production and oxidation rates [10]. Recently, the effect of different solvents on signal intensity was investigated [11], and it was shown that acetone and methanol provide higher signal levels as compared to water. Irrespective of the solvent, the production of Indium atoms is limited to regions with high temperature, $T > 1,000$ K. Potential problems induced by the use of solvents for seeding can be circumvented by use of a laser ablation seeding source [12]. This requires an additional laser and also should not be used with air as carrier flow.

In this work, a new seeding method has been developed, in which InCl₃ salt is mixed with micron-size alumina particles (Al₂O₃) and then fed into the flame by means of a modified PIV seeding system. This method provides fast salt decomposition at small particle seeding rates, making this methodology truly non-intrusive and allows obtaining strong TLAF signals without flame perturbation, even in lean flames.

Below, we will present data on thermometry in lean flames on a Bunsen-type multi-slot burner. We realize that this is not the kind of flame for which TLAF would be most beneficial. After all, this flame is lean and stable, and temperature distributions could also be obtained by techniques that require scanning (e.g., CARS) or substantial averaging (e.g., Rayleigh scattering). It is, however, a flame currently under detailed study in our lab and serves well to develop the technique. In TLAF measurements for temperature, the basic idea is to correlate the Stokes and anti-Stokes fluorescence ratios in a three-level system to flame temperature. The ratio of the measured fluorescence intensities reflects the population ratio of the two closely spaced spin-orbit components of the atomic ground state, which is governed by Boltzmann statistics. In most studies, the relationship between the excitation power and collected fluorescence is considered to be linear and it is also assumed that the level populations are in steady state during the entire excitation pulse. The extent to which those assumptions are valid does not seem to have been studied before (or at least it is not reported in the literature). Recently, Medwell and coworkers extended the TLAF method to the nonlinear regime [5], which already implied a significant gain in signal, albeit it at the expense of a more complicated calibration procedure. In this paper, we will consider the possibility of working in the fully saturated regime, in which the LIF yield does not depend on excitation pulse energy any more.

An immediate benefit of working in the saturation regime is the maximized fluorescence yield which results in more signal, so hopefully in more accurate temperature estimation and single-shot measurements. This would be very interesting for turbulent combustion applications, where the temperature profile may change on a very short time scale. Another advantage of the saturation regime is the reduced sensitivity for pulse-to-pulse fluctuations and non-uniformity of the laser irradiance. In the limit of full saturation, the generated fluorescence becomes completely independent of irradiance variations, and the TLAF method becomes immune to such fluctuations. Thus, reaching the saturation level over the whole field of view means that there would be no requirement for monitoring of the excitation laser spatial profile and subsequent image corrections. On the other hand, spectral interference, especially in the case of sooting flames [13], will become more of an issue. More fundamentally, level populations would, in the saturation regime, be strongly perturbed from their initial values, and it is not obvious that the fluorescence intensity ratio can still be used as a proxy for temperature. This latter aspect will be dealt with below.

2 Theory and simulations

The theoretical treatment of the TLAF problem over the full excitation strength range requires a solution of the pertinent rate equations. Although these equations are linear, a manageable analytical solution exists only for square excitation, that is, a constant-intensity light pulse that switches on and off instantaneously (Zizak et al. [14]). For a practical laser pulse, such a model is not very realistic, and moreover the analytical solution is still quite complicated, and does not yield much insight. This is compounded by the fact that we do not know all the relevant relaxation rates in the system. These parameters are decisive for the behavior of level populations, which in turn determine the fluorescence rates.

Our calculations are based on numerical solutions of the general rate equations for a three-level system, as described in detail by Zizak et al. [14]. Since we will be interested especially in the response of the system under strong excitation, a first question to be answered is whether the use of rate equations, rather than a more comprehensive approach that takes coherence into account, like the optical Bloch equations (e.g., [15]), is still a valid approach. As a general rule, rate equations are valid when either the bandwidth of the excitation is large relative to the transition line widths, or the collision- and Doppler-broadened line width is much larger than the natural line width [16]. In the present case, the former condition is not necessarily fulfilled, but the second one is, given that the natural width of both transitions of interest amounts to about 100 MHz. Thus, the rate

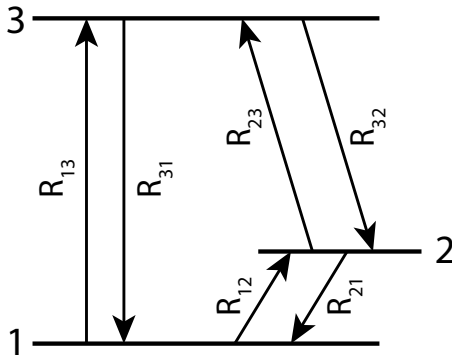


Fig. 1 The general three-level system and the transition rates involved. In the case of the In atom, levels 1 and 2 make up the spin-orbit-split electronic ground state

Table 1 Rate constants for the two excitation processes in TLAF

Stokes (3 ← 1 excitation)	Anti-Stokes (3 ← 2 excitation)
$R_{13} = B_{13}E_{13}$	$R_{13} = 0$
$R_{31} = B_{31}E_{13} + Q_{31} + A_{31}$	$R_{31} = Q_{31} + A_{31}$
$R_{23} = 0$	$R_{23} = B_{23}E_{23}$
$R_{32} = Q_{32} + A_{32}$	$R_{32} = B_{32}E_{23} + Q_{32} + A_{32}$

See also Fig. 1 and the text for explanation

equation approach is expected to be valid for the case of interest here.

Briefly, we consider a three-level system with transitions, described by rate constants, between any level pair (Fig. 1). The transitions can be due to anything, collision- or light-induced, and the associated rate constants R_{ij} , for a transition $i \rightarrow j$, may be time dependent (for a contribution due to a laser pulse, for instance). We will describe the level populations in terms of fractional populations $n_i(t)$, for which the rate equations take the form

$$\begin{aligned} \frac{dn_1}{dt} &= -(R_{13} + R_{12})n_1 + R_{31}n_3 + R_{21}n_2 \\ \frac{dn_2}{dt} &= -(R_{23} + R_{21})n_2 + R_{32}n_3 + R_{12}n_1 \\ \frac{dn_3}{dt} &= -(R_{31} + R_{32})n_3 + R_{13}n_1 + R_{23}n_2 \end{aligned} \tag{1}$$

Table 2 Properties of atomic Indium and the levels we use for TLAF experiments

Lower level	Air λ (nm)	A_{3j} (MHz)	E'' (cm^{-1})	E' (cm^{-1})	Designation	g''	g'
1	410.176	56	0	24,372.956	[Cd]5p-6s	2	2
2	451.131	102	2,212.598	24,372.956	[Cd]5p-6s	4	2

Data from the NIST Atomic Spectra Database [23]. g Denotes level degeneracy

we will take the thermal Boltzmann fractions as initial conditions and assume the 3-level system to be closed, that is

$$n_1(t) + n_2(t) + n_3(t) = 1 \quad \forall t, \tag{2}$$

so that the set of rate equations can be reduced to, for instance,

$$\frac{dn_2}{dt} = R_{12} - (R_{21} + R_{23} + R_{12})n_2 + (R_{32} - R_{12})n_3 \tag{3}$$

$$\frac{dn_3}{dt} = R_{13} + (R_{23} - R_{13})n_2 - (R_{31} + R_{32} + R_{13})n_3 \tag{4}$$

For the particular case of TLAF, transitions between levels 1 and 2 are dipole-forbidden. We will assume them to be collision-induced and relate the downward and upward rates through detailed balancing [17, 18], that is,

$$\frac{R_{12}}{R_{21}} = \frac{g_2}{g_1} \exp\left(-\frac{\Delta E}{k_B T}\right), \tag{5}$$

in which the g_i are level degeneracies and ΔE is their energy difference. Two separate fluorescence measurements need to be considered. For the Stokes fluorescence, we excite $3 \leftarrow 1$ and monitor $3 \rightarrow 2$, whereas for the anti-Stokes fluorescence, we excite $3 \leftarrow 2$ and monitor $3 \rightarrow 1$. The rate constants pertinent to both situations are listed in Table 1. They are expressed in terms of the Einstein A and B coefficients for spontaneous and induced radiative transitions, respectively, and the collision-induced quenching rate coefficients Q . The spectral energy density of the incident radiation is denoted by E , and subscripts indicate the individual transitions, as above. Some of the relevant parameters for the Indium atom are summarized in Table 2.

A Gaussian excitation laser pulse with duration $\tau = 10$ ns is assumed, that is,

$$P(t) = \frac{E_0}{\sqrt{2\pi}\tau} \exp\left(-\frac{t^2}{2\tau^2}\right), \tag{6}$$

in which $P(t)$ is the instantaneous laser power and E_0 is the total pulse energy. The spectral bandwidth is assumed to be 3 GHz (manufacturer specification) and the beam is assumed to be formed into a light sheet of 120 mm² cross section (60 mm high, 2 mm wide). The total number of

generated spontaneous fluorescence photons after excitation is calculated by integrating $A_{31}n_3$ or $A_{32}n_3$ over time for the anti-Stokes and Stokes transitions, respectively. Note that the level population densities are normalized to total density and the calculated number of photons is therefore also normalized. This is illustrated in Fig. 2, which shows the generated number of photons for anti-Stokes and Stokes transitions in atomic Indium (at $T = 2,000$ K) as a function of excitation laser fluence.

Closer examination of Fig. 2 reveals two facts. First of all, the generated number of Stokes photons upon 410 nm excitation is considerably higher than that of anti-Stokes photons upon 451 nm excitation, under otherwise similar conditions. At low pulse energies, this is mainly due to the higher population density in the lowest ground state. Moreover, the rate at which the generated number of photons reaches saturation is faster with 451 nm excitation in comparison with 410 nm. In saturation, the deterministic parameter is the ratio of stimulated to spontaneous transitions. For 410 nm excitation, this parameter amounts to $B_{31}/(A_{32} + A_{31}) = 1.4 \times 10^{12} \text{m}^3 \text{J}^{-1} \text{s}^{-1}$ and for 450 nm it takes a higher value $B_{32}/(A_{32} + A_{31}) = 3.5 \times 10^{12} \text{m}^3 \text{J}^{-1} \text{s}^{-1}$ [8]. As we will see later, this will be confirmed by experiments.

Figure 3 shows typical results for the two different excitation regimes. It shows the temporal behavior of all level populations, upon 410 nm excitation ($3 \leftarrow 1$). In the linear regime (albeit with a laser pulse energy that is already a bit high: level populations change by about 10 %), the upper level population follows the laser pulse, and so does the fluorescence yield. In this case, the fluorescence ratio will directly reflect the population ratio of the lower states. The decay kinetics of the upper level determines the fluorescence signal intensity and by increasing the excitation energy the transition from the linear regime to saturation becomes visible. This is confirmed by the fact that in saturation the transient population of the third level deviates from the Gaussian excitation profile and it levels off at high laser intensities. One interesting point is the coupling of the ground levels; they both experience a similar variation during excitation. This is due to the fast ground-state relaxation term, R_{21} , which tries to force the level populations into thermal equilibrium. For example, in Fig. 3, the excitation couples the first and third level, but the population of level 2 is also decreased. This term also helps the ground-state populations to recover after excitation.

In order to investigate the effect of the ground-state relaxation rate, R_{21} , we repeat the calculations of Fig. 3 with R_{21} reduced by two orders of magnitude, that is, $R_{21} = 0.1A_{32}$. The results are shown in Fig. 4. As expected, it takes longer for the ground levels to reach equilibrium after excitation. Upon strong excitation (panel b) the

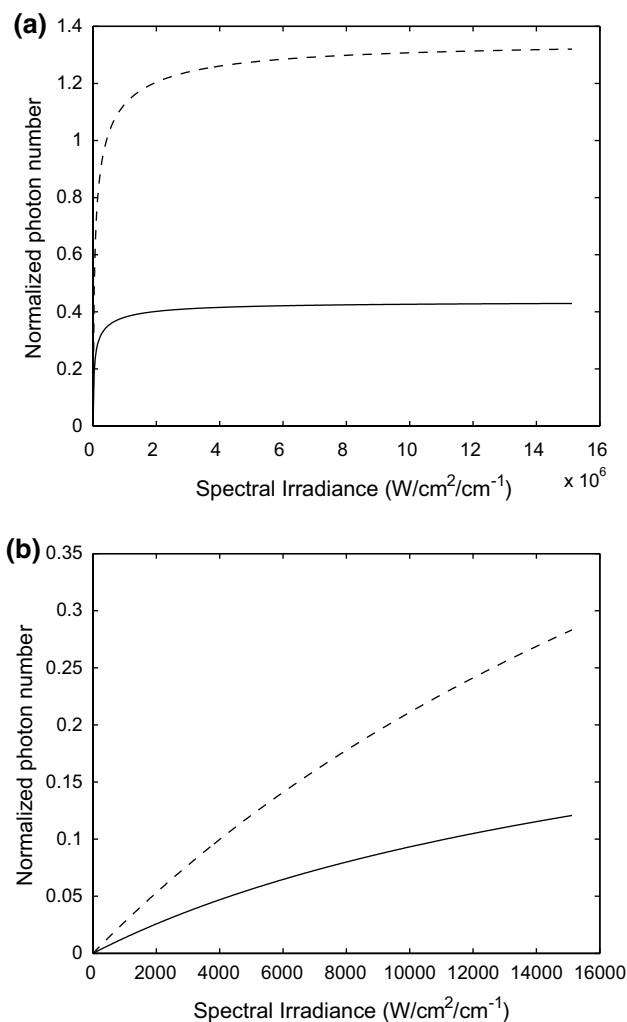


Fig. 2 **a** The generated fluorescence photon number as a function of pulse energy for 451 nm excitation (anti-Stokes fluorescence detection; *solid lines*) and 410 nm excitation (Stokes fluorescence detection; *dashed lines*). The laser pulse profile is assumed to be Gaussian with duration of 10 ns (FWHM) and spectral band width of 3 GHz. **b** Zoomed in to show the approximately linear region. See text for details

excited state population n_3 now shows an initial peak, followed by a decline. The latter is due to population slowly being trapped in the level that is not pumped by the excitation laser. Contrary to Fig. 3 in which the decay rate out of level 2 was faster than the fluorescence rate into it, the population in level 2 is now (Fig. 4) seen to increase during the laser pulse. Note that the speed of ground-state relaxation (thermalization) is governed by R_{21} and R_{12} , which are now considerably reduced relative to the situation of Fig. 3.

We have tried to estimate the fluorescence lifetime experimentally. In this experiment, we recorded the laser intensity (elastic scattering) and the fluorescence intensity as a function of time by changing the delay between the laser trigger and the ICCD gate in steps of 5 ns. The camera

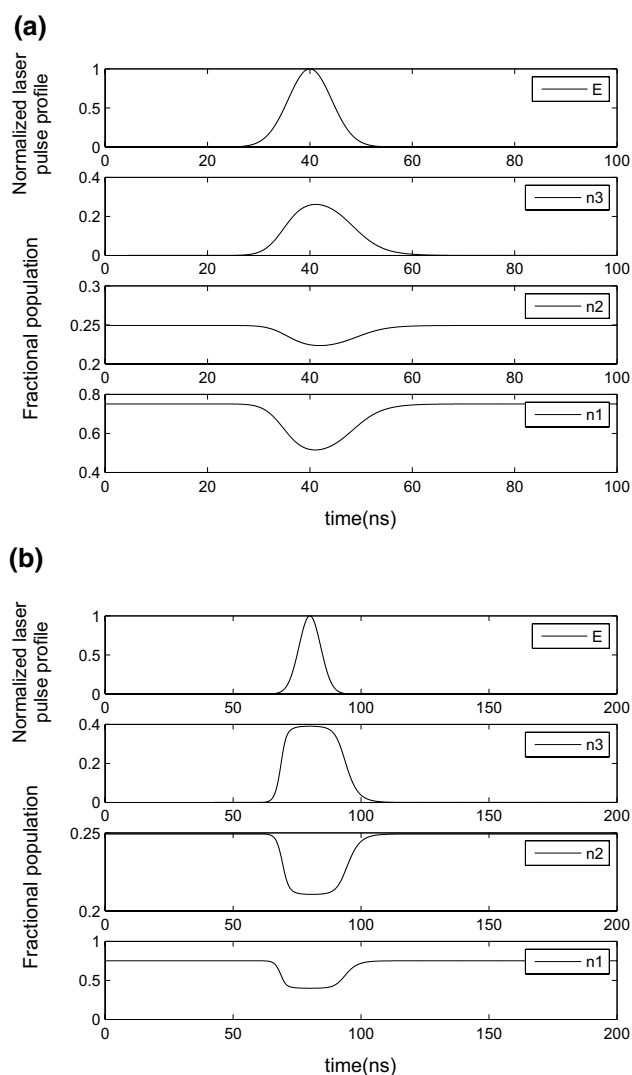


Fig. 3 Calculated temporal behavior of level populations in atomic Indium after excitation at 410 nm ($1 \rightarrow 3$) by a gaussian laser pulse of 10 ns width (FWHM), for **a** linear and **b** saturation regime. We used the following parameters in the calculations: $R_{21} = 10A_{32}$, $Q_{32} = A_{32}$, $Q_{31} = A_{31}$, $E_{lin} = 0.1$ mJ and $E_{sat} = 4$ mJ. Note the vertical scale differences between the various panels

gate width was kept fixed at 50 ns. Although the exact time profile of the opening of the image intensifier gate is not known, we expect the opening edge to be steeper than the closing one. Thus, in this experiment, the fluorescence is sampled by something that resembles a square gate, that itself lasts much longer than the fluorescence and is stepped in 5 ns steps over the fluorescence time profile. As shown in Fig. 5, the fluorescence intensity more or less follows the laser pulse. It does not ‘almost precede’ the laser pulse as in the simulation of Fig. 3b, but neither does it show an initial maximum as in Fig. 4b.

The ground-state relaxation rate in the Indium atom is one of the parameters that we do not have enough

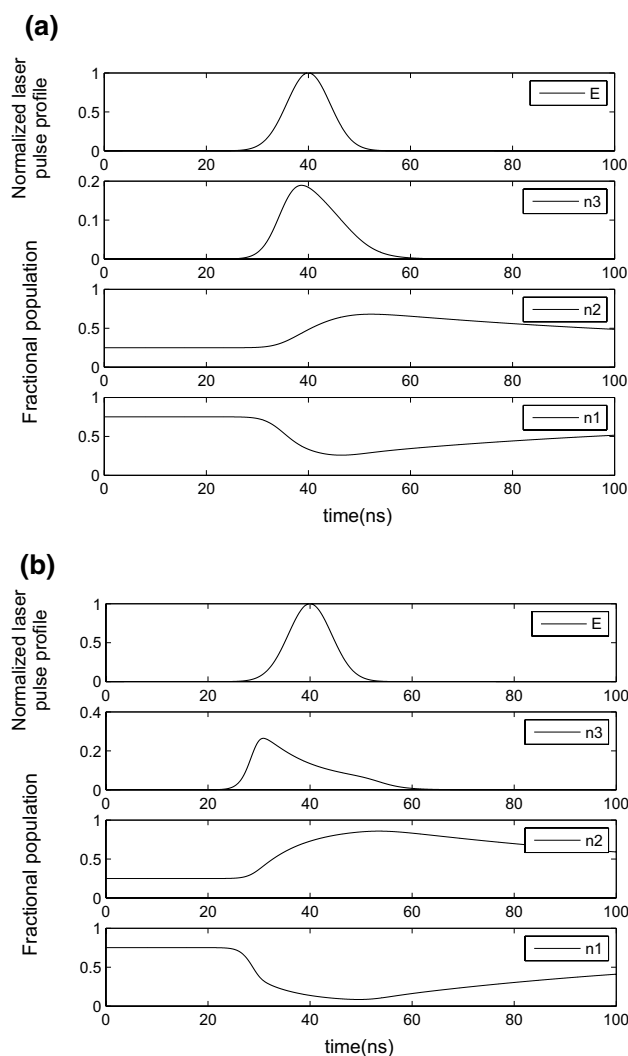


Fig. 4 As Fig. 3, but $R_{21} = 0.1A_{32}$

knowledge of, and with this simulation and the comparison with our experimental evidence, we conclude that R_{21} is in the order of or somewhat larger than the spontaneous emission rates.

2.1 Temperature estimation in the saturation regime

Using TLAF in the saturation regime (saturated TLAF, or sTLAF) requires a model that describes the process, and our final goal here is to find an equation to calculate the temperature from measured fluorescence signals. Based on Fig. 3, we assume steady state during the whole pulse in the saturation regime and solve the rate Eqs. 3 and 4 for the upper level population under conditions of heavy saturation, using the rate constants from Table 1 for the two excitation schemes. Taking degeneracies into account, we have $B_{13} = B_{31}$ and $B_{32} = 2B_{23}$. For 410 nm excitation ($3 \leftarrow 1$) the steady-state solution for n_3 becomes

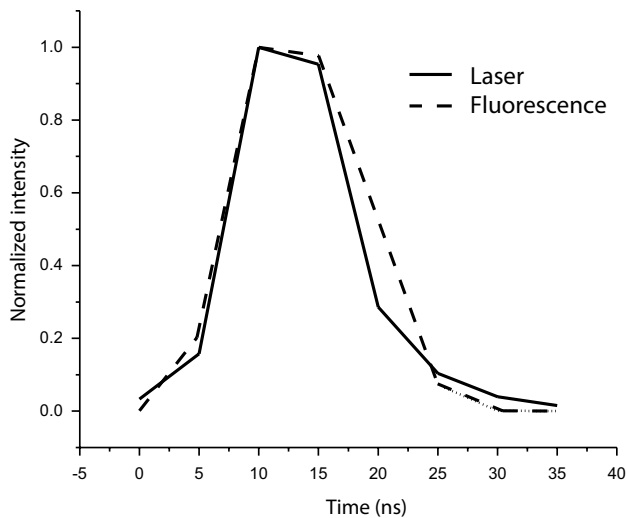


Fig. 5 Normalized intensities of the excitation laser and the induced fluorescence as a function of time delay between laser pulse and camera gate opening. $t = 0$ is arbitrary

$$n_3^{(13)} = \frac{R_{21}}{Q_{32} + A_{32} + R_{12} + 2R_{21}} \quad (7)$$

and the fluorescence yield ($3 \rightarrow 2$) is (in this steady-state approximation) given by

$$F_{32} \propto A_{32} n_3^{(13)} \tau_{13} = \frac{A_{32} R_{21} \tau_{13}}{Q_{32} + A_{32} + R_{12} + 2R_{21}}, \quad (8)$$

in which τ_{13} is the pulse duration of the excitation laser.

Similarly, for 451 nm excitation ($3 \leftarrow 2$) the steady-state solution for n_3 becomes

$$n_3^{(23)} = \frac{R_{12}}{Q_{31} + A_{31} + 3R_{12} + 2R_{21}} \quad (9)$$

and the fluorescence yield ($3 \rightarrow 1$) follows as

$$F_{31} \propto A_{31} n_3^{(23)} \tau_{23} = \frac{A_{31} R_{12} \tau_{23}}{Q_{31} + A_{31} + 3R_{12} + 2R_{21}}, \quad (10)$$

in which τ_{23} is the pulse duration of the (other) excitation laser.

For the fluorescence ratio, we then find a somewhat complicated expression,

$$\frac{F_{31}}{F_{32}} = \frac{A_{31} \tau_{23}}{A_{32} \tau_{13}} \frac{Q_{32} + A_{32} + R_{12} + 2R_{21}}{Q_{31} + A_{31} + 3R_{12} + 2R_{21}} \frac{R_{12}}{R_{21}}. \quad (11)$$

In the largest fraction, the rate constants occur as a sum. From the temporal shape of the fluorescence, it looks as if R , A and Q are of the same order of magnitude, so as a first approximation we take this fraction to be temperature independent. Calling it D , and using the detailed balancing relation 5 between R_{12} and R_{21} , we find

$$\frac{F_{31}}{F_{32}} = \frac{A_{31} \tau_{23}}{A_{32} \tau_{13}} D \frac{g_2}{g_1} \exp\left(-\frac{\Delta E}{k_B T}\right), \quad (12)$$

from which follows that

$$\frac{\Delta E}{k_B T} = \ln \frac{F_{32}}{F_{31}} + \ln \frac{A_{31}}{A_{32}} + \ln \frac{\tau_{23}}{\tau_{13}} + \ln 2D. \quad (13)$$

Thus, we end up with a temperature equation that is quite similar to the one used in the linear regime [19], but due to our assumptions the calibration constant will now also possess some temperature dependence.

Interestingly, the temperature derived from TLAF in the saturation regime is qualitatively different from the one measured in the linear regime. In order to explain this, let us revisit the rate equations, Eq. 1. Temperature is in there in two ways: via the initial level populations, and via the detailed balancing relation between the two ground-state relaxation rate constants, Eq. 5. In the linear regime, the fluorescence yield is directly proportional to the initial level populations, and the ground-state relaxation rates are irrelevant. Thus, the fluorescence ratio is essentially the population ratio, and this is translated into a temperature. From Fig. 3b, however, it is clear that in saturation during most of the fluorescence lifetime the populations are heavily perturbed from their initial values. In fact, the population distribution during the excitation pulse is largely determined by the ground-state relaxation process (compare panels b in Figs. 3 and 4). The temperature involved here is a gas kinetic one that determines the relative magnitude of the forward and backward relaxation rates between the two ground states. In thermal equilibrium, these two temperatures are equal, but in non-equilibrium situations they need not. For combustion processes, it might be argued that the gas kinetic temperature measured by saturated TLAF is the more relevant one.

In order to investigate the validity of our assumption of invariant populations during excitation, and the thus derived equation for temperature, a simulation is performed for a given temperature and calculating F_{32} and F_{31} . We then estimate the temperature using equation 13. The simulation is repeated with different values of thermal relaxation rate R_{21} and quenching rate Q , but we always use the same calibration constant, determined at a reference temperature of 1,500 K, in the temperature estimated by Eq. 13. This is to investigate the effect of these parameters on temperature estimation and its sensitivity to variation of these parameters. The simulation is performed over a 500 K temperature range where the central temperature is set to 1,500 K. The results are shown in Figs. 6 and 7. Figure 6 shows the relative error in temperature estimation as a function of temperature and thermal relaxation rate R_{21} for the case of $Q = A_{32}$. Similar

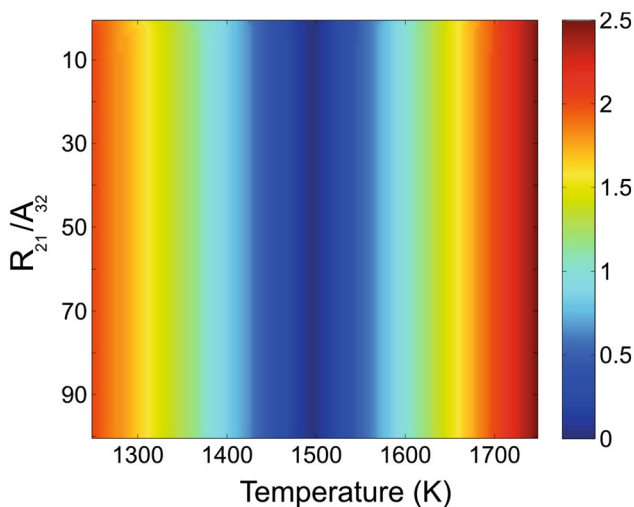


Fig. 6 The relative error of temperature estimation as a function of thermal relaxation rate, for $Q = A_{32}$. The *color bar* represents error percentages

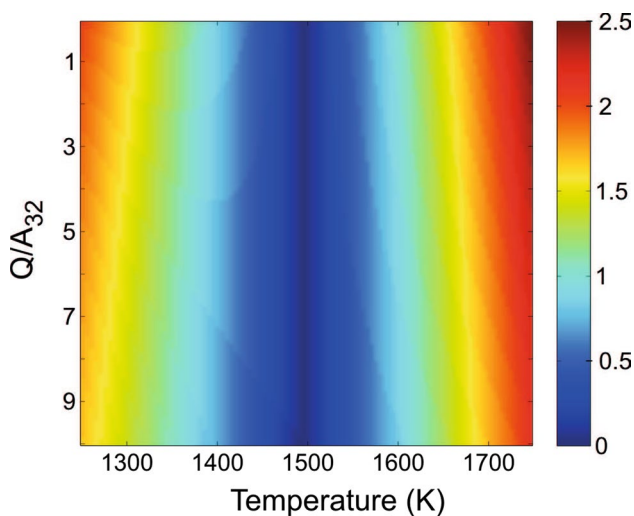


Fig. 7 The relative error of temperature estimation as a function of quenching rate Q , for $R_{21} = A_{32}$. The *color bar* represents error percentages

calculations for $Q = 10A_{32}$ and $Q = 0.1A_{32}$ yield similar results (not shown). Upon varying the temperature from 1,250 to 1,750 K, the maximum relative error is found to be 2.5 %. Moreover, no obvious variation in relative error is observed by changing the quenching rate: the error is a function of temperature itself. This means that in a non-uniform flame with a maximum variation of temperature of 500 K the maximum relative error that is due to taking a temperature-independent calibration factor amounts to 2.5 %. In many practical applications, the temperature variation will typically be less than that.

3 Optical setup and data processing

The experimental setup, Fig. 8, comprises two pulsed Nd:YAG lasers (Spectra Physics) with 10 Hz repetition rate. The third harmonic of each laser is launched into one of two dye laser systems (Sirah Precision Scan), operated on either Exalite 411 or Coumarine 2 to generate the desired wavelengths for the TLAF experiment, 410 and 451 nm, respectively. Their spectral bandwidth amounts to about 3 GHz (manufacturer specification), whereas the Doppler- and pressure-broadened absorption linewidths are about 10 GHz. A combination of a cylindrical and a spherical lens is employed to make light sheets with approximate size of $2 \times 60 \text{ mm}^2$, covering the full flame height. Weak spatial filtering followed by a rectangular aperture is used to clip each beam, so as to reduce wing effects and to reach full saturation over the whole field of view. Fluorescence emission is captured by one of two ICCD cameras (Roper PIMAX 3), equipped with either a band pass filter ($448 \pm 10 \text{ nm}$) or a short pass filter (440 nm cutoff; both Semrock) to reject the elastic scattering at wavelengths of 410 nm and 451 nm, respectively. The cameras and lasers are triggered by two delay generators (SRS DG535). The lasers are fired with a delay of 100 ns. This time scale is short compared to the characteristic time scales of the flame (see below). The ICCD cameras are gated, and the gate duration is around 50 ns. This small gate width reduces collection of background signal.

3.1 Seeding system and flame

Figure 9 shows a schematic of the burner used in the experiments, with gas supply, seeding, and thermostating systems. The burner was designed to study flame cusps formed in flames of ultra-lean mixtures, in particular for hydrogen-methane-air mixtures. The cusps are represented by tips of 2D burner-stabilized Bunsen flames. The burner has seven slots of $4 \times 40 \text{ mm}^2$ cross section, separated by 4 mm distance. The cameras are aligned parallel to the slots. A multi-slot configuration was chosen for the burner because of two reasons. First, due to the mutual support of the flames, much leaner flames can be stabilized on such a burner than would be possible with a single-slot burner. Second, the three central flames stabilized on the burner are nearly identical, which allows simplifying the (planned) numerical simulations of these flames by applying periodic boundary conditions. Premixed fuel and air is supplied to the burner plenum chamber where it is evenly distributed among slots and along each slot using a plate with double rows of equally spaced 0.5 mm diameter holes positioned along each slot entrance.

A wire mesh roll surrounding the mixture inflow port is installed in the plenum chamber to quench turbulence inside

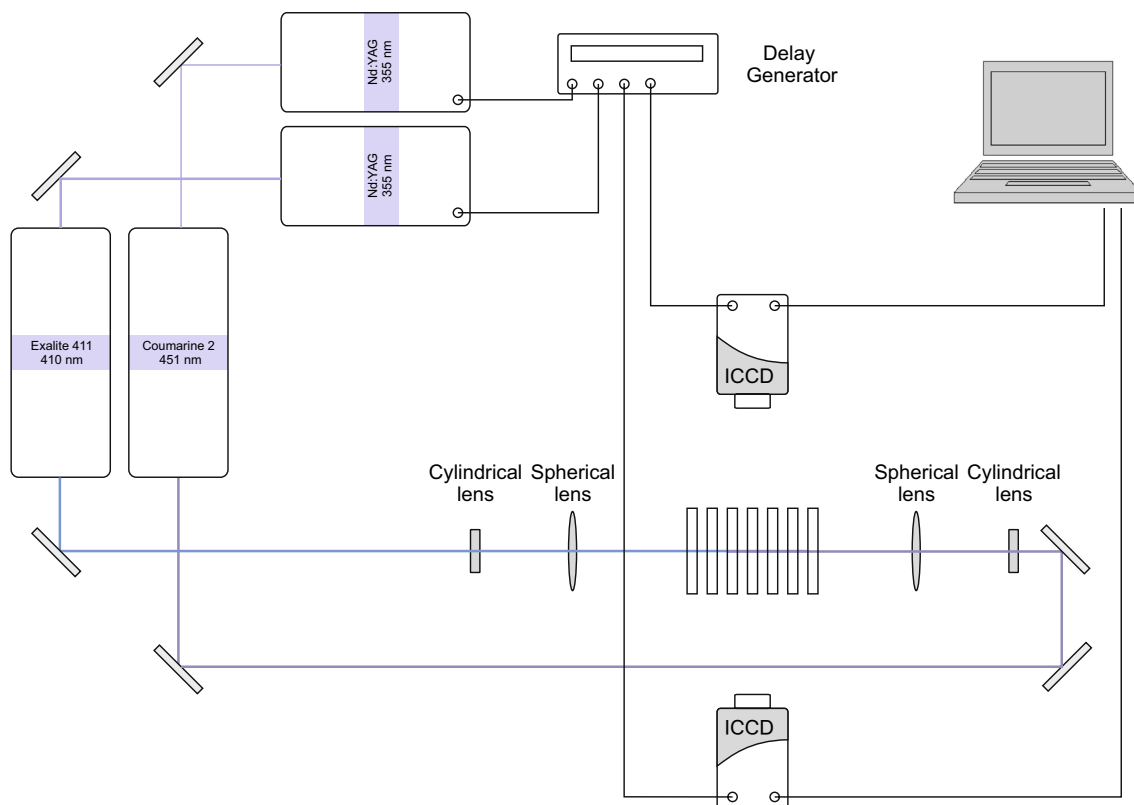


Fig. 8 Schematic diagram of the TLAF setup. The *vertical bars* between the two cameras represent the multi-slot burner

the chamber and to remove possible pressure pulsations, which otherwise would disturb the flames. Flow straighteners are installed inside each slot just before the exit to laminarize the flow after passing through the small holes in the flow distribution plate, and to form near-uniform mixture velocity profiles at the burner exit. Flames formed above the two edge slots are anchored to the burner only at one, inner, side. If no special precautions are taken, periodic vortices form above these flames and disturb these and all other flames. To render the flame stable, a duct made of fused silica plates is installed above the burner outflow plane. Besides removing the above-mentioned vortices, the duct protects the flames from occasional drafts and improves flame anchoring to the burner, extending thereby the range of mixture equivalence ratios for which a flame can be stabilized. Two side plates of the duct are slightly inclined outward, as it was found empirically that inclining these plates was required for the central flames to be near-identical. The duct is covered with a metal grid which helps to remove instabilities related to natural convection. The burner surface is kept at constant temperature (45 °C) using thermostated water flow, which is pumped through the channels drilled between neighboring slots and along the burner perimeter.

High-purity cylinder gases (hydrogen, methane, and dry synthetic air) were used for preparing the desired fuel/air

mixtures. These mixtures were prepared in-line with the help of three mass flow controllers installed in the individual gas lines. After combining all three flows, the mixture flow is split between two lines. One line is connected to a fluidized bed seeding system and the other one is a bypass line. The fraction of the total flow traveling through the bypass line is controlled by two needle valves installed in both lines after the flow splitting and monitored using a ball rotameter installed in the bypass line. By varying this fraction, the seeding density is varied. After recombining bypass and seeded flows, the mixture is directed to the burner plenum chamber. The fluidized bed vessel contains a mixture of InCl_3 salt and $1\ \mu\text{m}$ diameter Al_2O_3 particles, manually ground with mortar and pestle to achieve a uniform size distribution. It was mounted on a flexible support and shaken by a vibrating motor attached to the vessel, to prevent accumulation of seeding powder on the vessel walls. To keep the alumina seeding powder dry, a ring-like container with perforated walls was filled with silica gel and installed inside the fluidized bed vessel in its upper part. A piece of wide (2 cm diameter) tube, installed horizontally downstream of the fluidized bed, works as a gravity filter. Flow inside this tube is slow and laminar, allowing coarse particle agglomerates in the mixture to settle inside the tube.

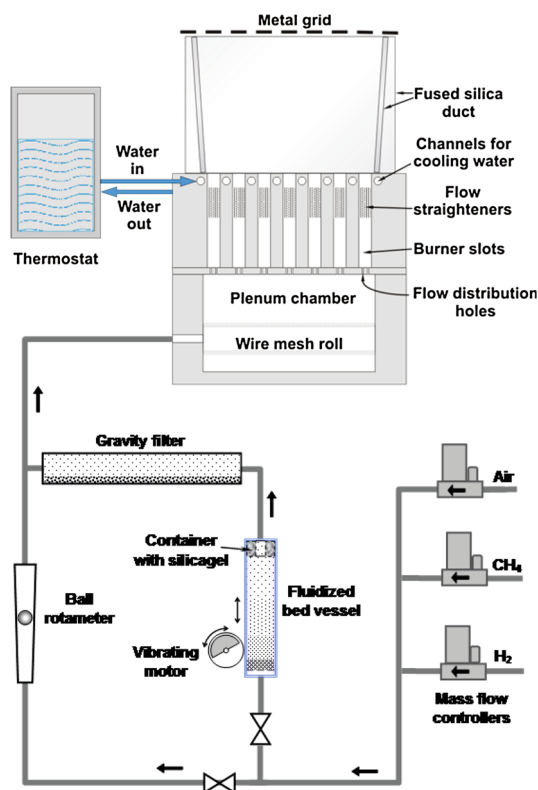


Fig. 9 Schematic diagram of the slot burner and seeding system (Design by Y. Shoshin.)

3.2 Image analysis

The recorded images were analyzed with a homemade code developed in Matlab. Registration (alignment) of the two images recorded by the two ICCD cameras is also performed in Matlab, with the help of a calibration image: a metal plate with four holes close to its edges was illuminated uniformly from the back side and the image was recorded by both cameras. The transformation matrix is determined, and we used this matrix to transform the fluorescence image of 410 nm. This transformation includes affine and projective transformations, which correct the camera mismatch. The initial analysis, comprising background subtraction, Gaussian filtering and speckle removal, are performed in ImageJ [20].

The cameras are flatfield-corrected by recording the image of a white diffuser sheet illuminated from the back. For measurements in the fully saturated regime a laser profile correction is not needed, but for linear regime experiments we recorded the laser beam profile by imaging the fluorescence of a cuvette at the position of the burner, but filled with dilute Rhodamine-B solution and excited by either 410 or 451 nm radiation.

In TLAF, absorption of (especially the anti-Stokes) fluorescence by the seeded In-atoms themselves is a matter of

concern. We have checked the effect of self-absorption by varying the position, along the line of sight of the cameras, at which the laser beams cross the flames. No effect of this location on the signal strength was found. Apparently, in the present setup, self-absorption plays no role of importance, possibly due to low seeding density and spatial extent of the Indium atom distribution (see below), in combination with the large collection solid angle of the camera optics.

3.3 Temperature calibration

In order to determine the calibration parameter for (saturated) TLAF experiments, the temperatures in two regions of the flame are measured with an S-type thermocouple (bead size 150 μm), and the measured temperature is corrected for conduction and convection heat losses. One of the points is used for calibration, and the other point is used for testing the validity of the TLAF experiment by comparing the temperature measured by the thermocouple to those from the TLAF experiment. In general, we expect the flame tip to show a lower temperature than the sides, because fuel gas mixtures containing hydrogen can be characterized by an effective Lewis number less than unity. According to flame stretch theory [21], a negative flame stretch rate at the flame tip should lead to reduced flame temperature.

4 Results

4.1 Saturation curves

In order to estimate the required intensity to reach the saturation regime, fluorescence images of the flame excited by 410 and 450 nm, respectively, are recorded and analyzed for different excitation pulse energies. The intensity of fluorescence images at different excitation energies are integrated to provide the total fluorescence intensity. The background level is calculated by binning a fluorescence-free region upstream of the flame, and subtracting this from the whole image. The result is depicted in Fig. 10. As expected, both fluorescence curves show a linear behavior at lower energies, and they reach a plateau at higher excitation energies, characteristic for the saturation regime. Note that the asymptotic behavior of the curves in Fig. 10 indicates that, in our experiments, the low-intensity wings of the laser beams apparently have been suppressed sufficiently well so as not to inhibit reaching the saturation regime. While the excitation on the 451 nm transition (Fig. 10a) reaches saturation at about 0.4 mJ/pulse ($\approx 0.11 \text{ MW}/\text{cm}^2/\text{cm}^{-1}$), the other transition starts to saturate only after almost 1.0 mJ/pulse ($\approx 0.28 \text{ MW}/\text{cm}^2/\text{cm}^{-1}$). These irradiance values

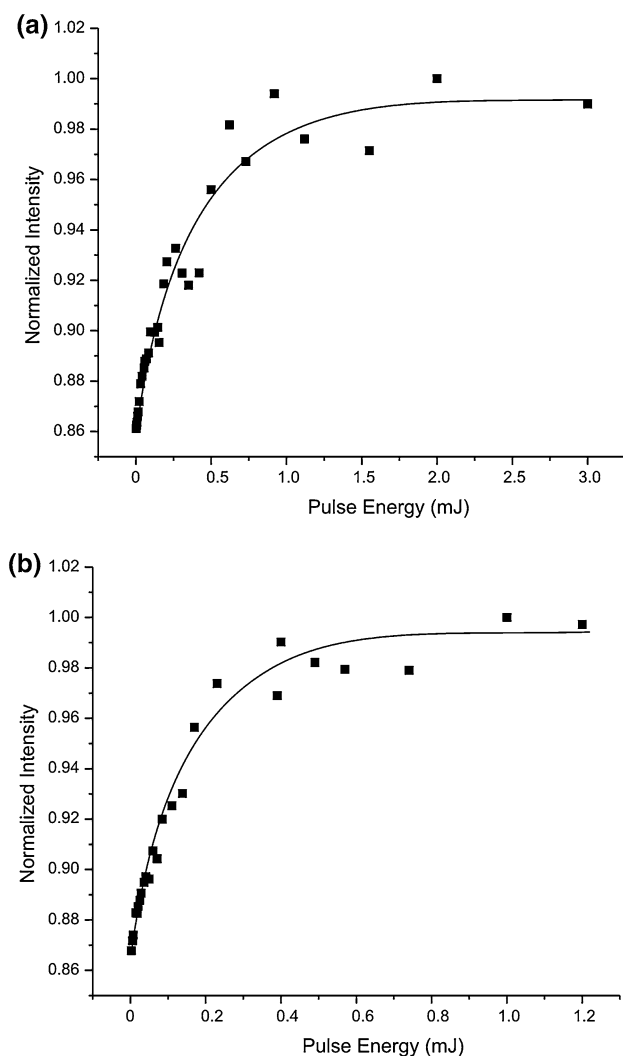


Fig. 10 Saturation curves for excitation at **a** 410 nm and **b** 451 nm. Note the different scales on the horizontal axes. Each data point corresponds to the integrated intensity of a background-corrected LIF image, averaged over 100 laser shots

correspond well to those at which the calculated curves of Fig. 2 start to flatten. At the same time, however, they are several orders of magnitude below the irradiance values used by Medwell et al. [5], at which full saturation was still not reached. We consider the presence of low-intensity wings in the spatial profile of the laser beams along the line of sight toward the detector to be a likely cause for this apparent discrepancy.

The fluorescence intensity in the saturation regime should be independent of excitation energy. The fluctuations in fluorescence yield that are still present in Fig. 10 after reaching saturation pulse energies are attributed to variations in seeding concentration. We have found that the seeding quality benefits from using very fine powder and degrades with increasing ambient air humidity.

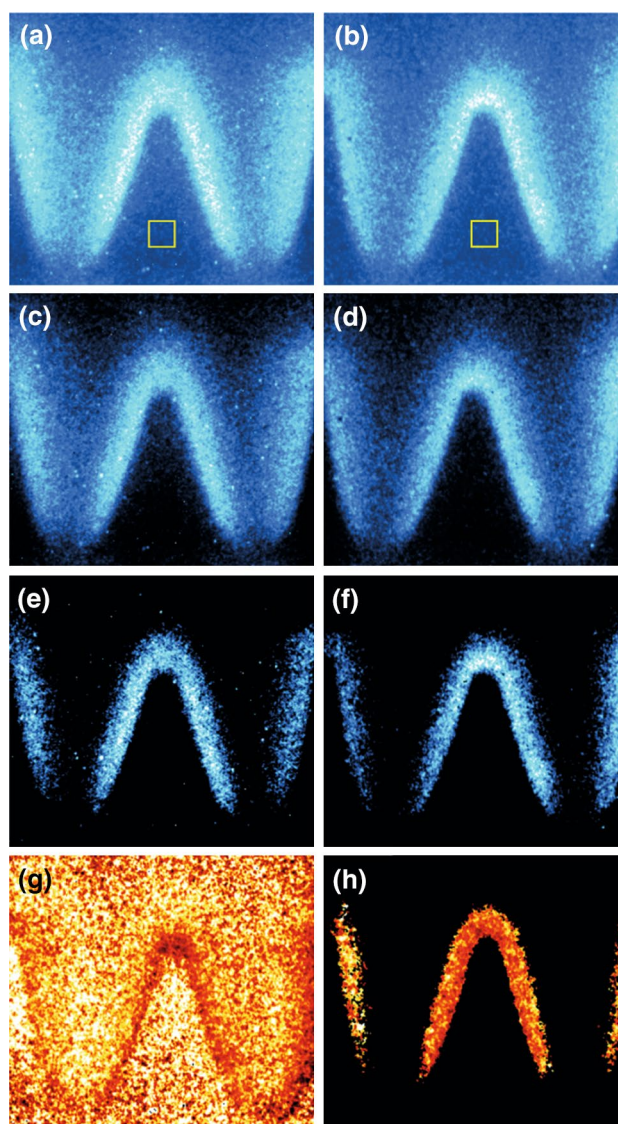


Fig. 11 Image processing steps for temperature estimation with sTLAF. LIF images at **a** 410 nm and **b** 450 nm fluorescence wavelength; signal-to-noise ratio is about 18. **c** and **d** The background subtracted images, for which the background signal is calculated by averaging the pixels in the yellow rectangles in panels **a** and **b**. **e** and **f** The thresholded images. Temperature images **g** without thresholding and **h** with thresholding. The analysis clearly benefits from thresholding the original images, before pixel-by-pixel division

4.2 Temperature images

Series of 100 single-shot fluorescence images each of a variety of flames with different equivalence ratios were recorded and analyzed. The process of analysis is illustrated in Fig. 11. From panels a and b in this figure, it is clear that the seeding density is far from uniform. Indium atoms are created in the flame front and disappear fairly quickly further downstream.

In this application, we are interested in fuel-lean flames, so there is considerable oxygen left downstream of the

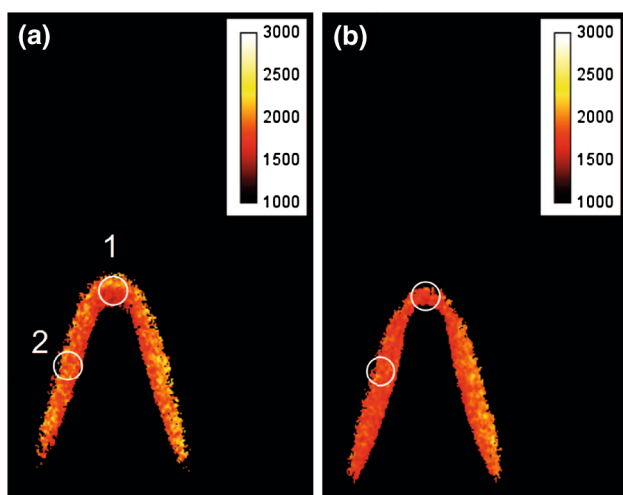


Fig. 12 Temperature images of two flames estimated by saturated TLAF for **a** $\phi = 0.711$, $u = 40$ mL/h; **b** $\phi = 0.674$, $u = 40$ mL/h. 4 single-shot images are accumulated for better signal

flame front, and In is expected to quickly become oxidized, thereby becoming invisible for the LIF system. (Although InO does have spectral bands in the region between the two wavelengths used here [22], we have seen no evidence of spectral interference at the exact wavelengths used for In-atom excitation.) The scattering observed away from the flame front is probably fluorescence that is elastically scattered by seed particles. We determine the background from a small region upstream of the flame front, in the cold gas, and subtract this value from the whole image. Since, like any ratio method, TLAF is susceptible to noise generated by the division of small numbers, we apply thresholding to evaluate the signals only in those locations where it is sufficiently strong. The resulting images are shown in Fig. 11, panels e and f. The fluorescence ratio image, finally, is shown in panel h. Panel g shows, as an example, the result if thresholding is omitted; the global flame structure can still be seen, but the noise produced by low-signal areas is also very obvious. In these regions, the signal is low and the shown results (panel g) are not reliable. The signal loss due to In oxidation is a particular issue for the fuel-lean flame studied here; in fuel-rich flames the In atom lifetime is much longer [3, 4].

Some of the results on a few of the flames actually studied are shown in Fig. 12: temperature distributions in two different flames. More results will be published elsewhere. The flame with equivalence ratio $\phi = 0.711$ burns on only methane and air, but the flame with $\phi = 0.674$ includes methane, air and hydrogen (20 % relative to methane, v/v). Laser energies are set to 2.5 mJ/pulse and 2.2 mJ/pulse for 410 nm and 451 nm excitation, respectively; sufficiently high to ensure that we perform the experiments in the saturation regime.

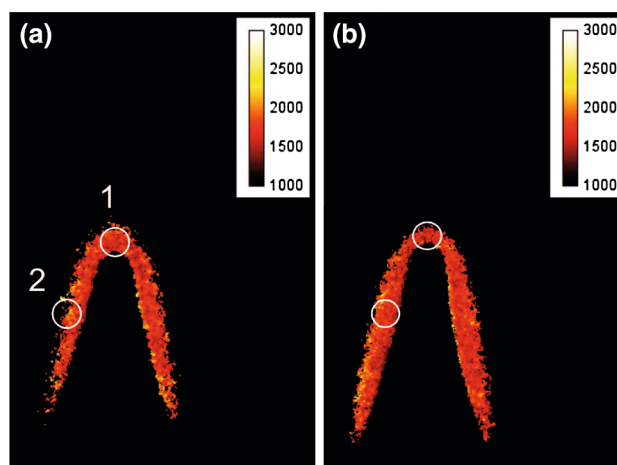


Fig. 13 Temperature images of two flames estimated with linear TLAF for the same flames as in Fig. 12. 4 Single-shot images are binned for better signal

Table 3 Temperature values (in K) for the labeled regions in Fig. 12

Flame	$\phi = 0.711$	$\phi = 0.674$
	$u = 40$ mL/h	$u = 40$ mL/h
Region 1 thermocouple T(K)	2,115	2,048
Region 1 sTLAF T(K)	2,119	2,045
Standard error	11	12
Region 1 TLAF T(K)	2,090	2,054
Standard error	17	14

Standard errors reflect pixel-to-pixel variation, rounded to above. Temperatures have been measured by S-type thermocouple, and by both saturated and linear TLAF

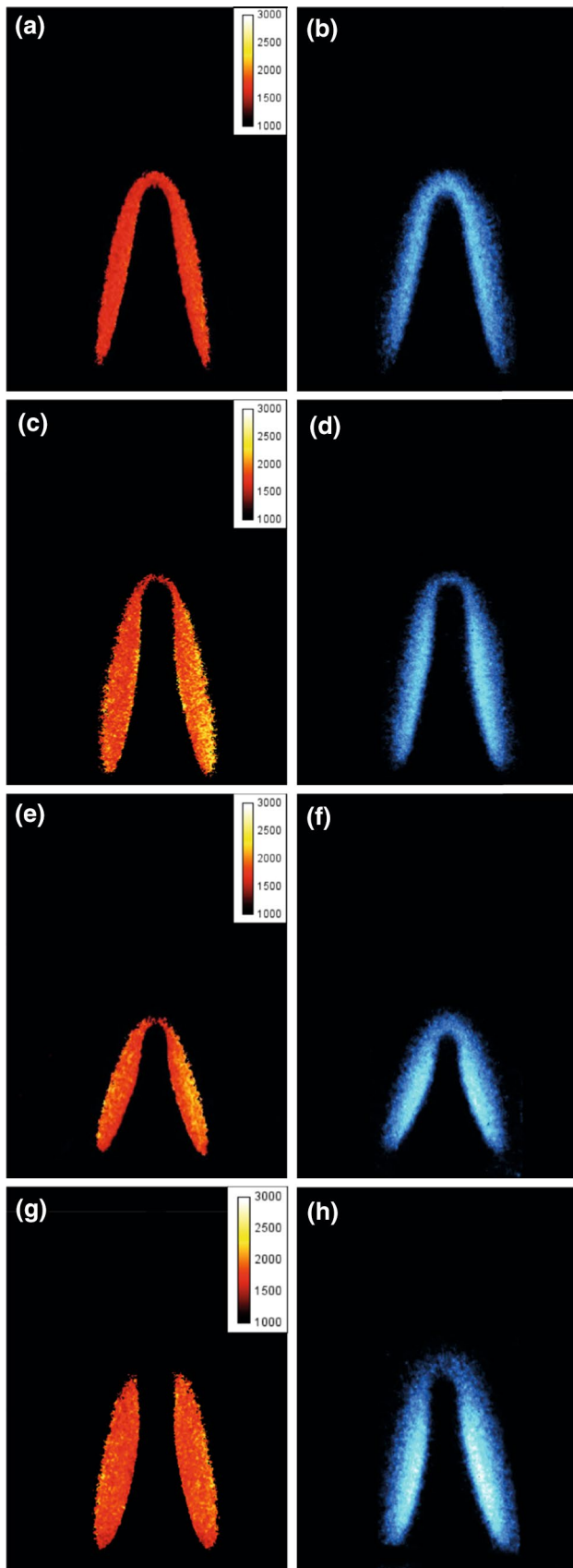
Table 4 Temperature results (in K) for various equivalence ratios and a constant flow rate of $u = 40$ mL/h, obtained by TLAF in the saturation regime and from thermocouple data

Flame	$\phi = 0.647$	$\phi = 0.631$	$\phi = 0.619$	$\phi = 0.58$
Region 1 T thermo-couple	2,260	1,969	1,931	1,838
Region 1 T sTLAF	1,991	1,944	1,915	n/a
Standard error	9	10	10	n/a

See text for the missing data in the last column

The temperature is measured for two regions, labeled in Fig. 12 by '1' and '2', each measuring 10×10 pixels. The temperatures in these two regions are also measured with a thermocouple, and region 2 is used to calibrate the measurements, as discussed above.

For comparison, we also show the result from TLAF using linear excitation in Fig. 13. The excitation energies are lowered to 0.08 mJ/pulse by means of a polarizing beamsplitter cube. Table 3 summarizes the estimated



◀ **Fig. 14** Temperature images four flames with cold gas flow velocity of $u = 40$ mL/h and equivalence ratios of **a** $\phi = 0.647$, **c** $\phi = 0.619$, **e** $\phi = 0.631$ and **g** $\phi = 0.58$. The corresponding fluorescence images at 451 nm are shown in panels **b**, **d**, **f** and **h**, correspondingly. The temperature information for $\phi = 0.58$ is missing in the flame tip due to very low fluorescence signal

temperatures from saturated TLAF and linear TLAF together with standard errors. The signal-to-noise ratio for linear TLAF is lower and the standard errors consequently higher in comparison with saturated excitation, but otherwise the results compare well. Imaging in the saturation regime provides higher signal and finally higher accuracy. The structure of the images, however, is the same in both cases.

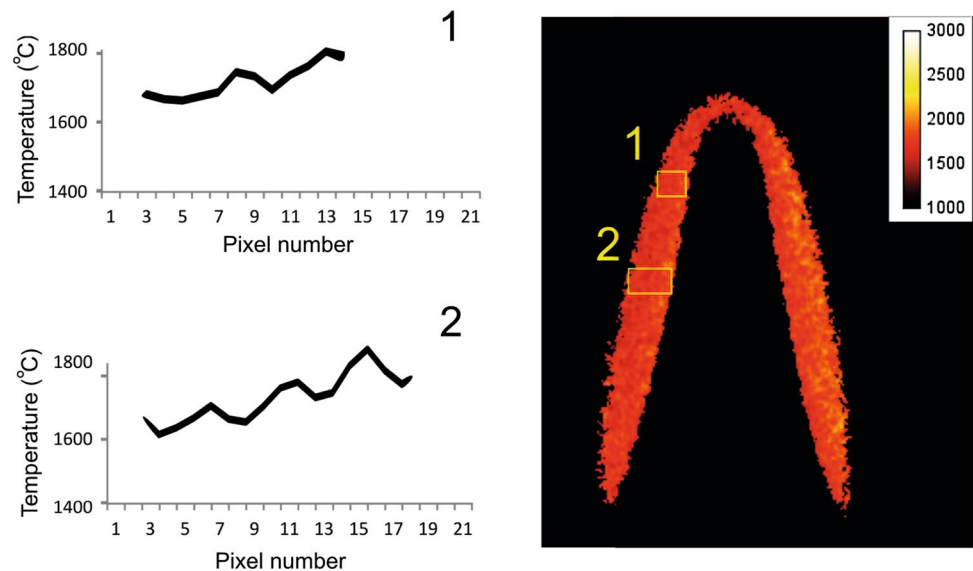
Fluorescence images of four flames with different equivalence ratios were recorded in the saturation regime and analyzed. The results are collected in Table 4. As before, region 2 is used for calibration and the temperature in region 1 is compared to the one from thermocouple measurements. The standard errors are also calculated.

The fluorescence intensity distribution obtained by 410 nm excitation, and the temperature images are shown in Fig. 14 for various equivalence ratios. The temperature image of $\phi = 0.580$ is not complete due to very low signal in the flame tip (region 1). This flame contains 40 % hydrogen. Figure 14 panels c and e show temperature images for flames with 20 % hydrogen. Figure 15 shows two horizontal temperature cross sections through the flame, vertically averaged over the areas indicated in the image. A slight temperature decrease from the flame front outwards can clearly be seen. Outside the clipping area, obviously, there is no temperature information.

5 Conclusion

We have developed a theoretical frame work for TLAF measurements in the saturation regime (saturated TLAF or sTLAF). Seeding of atomic Indium into the flame was achieved by means of a modified PIV seeding system, introducing alumina PIV seeding particles mixed with InCl_3 . The spatial extent of the In atom distribution in the fuel-lean flames studied here was found to be very limited. Complications due to non-saturating wings of the excitation laser beams (which would prevent reaching full saturation, even at much higher fluences than used in this paper) or self-absorption of the induced fluorescence were not observed. Atoms are produced in the flame front and apparently quickly oxidized further downstream. The method will appear to full advantage in rich flames, the more so because the laser irradiance required for full saturation are

Fig. 15 Temperature image of a flames with equivalence ratios of $\phi = 0.647$. The temperature cross section is shown for two different regions of interest shown on the temperature image



so low that attenuation of the laser light on its path through a possibly sooting flame can, to some extent, be accommodated. Self-absorption and spectral interference, however, may become an issue in more homogeneously seeded, rich flames. Temperature measurements based on single laser shots have been executed, resulting in relative uncertainties in the order of 10 K. This possibility can be very useful for turbulent combustion applications. Experimental results compare well to independent thermocouple measurements.

Acknowledgments The work of Y. Shoshin is supported by the Dutch Technology Foundation STW (Project 11616), which is part of the Netherlands Organization for Scientific Research (NWO), and which is partly funded by the Ministry of Economic Affairs.

References

- J. Lahaye, G. Prado, *Soot in Combustion Systems and Its Toxic Properties*. in Tech. rep., Center for Research on the Physico-Chemistry of Solid Surfaces CNRS (1983)
- K. Kohse, J. Jeffries, *Applied Combustion Diagnostics* (Taylor and Francis, London, 2002)
- J. Engström, J. Nygren, M. Aldén, C. Kaminski, *Opt. Lett.* **25**(19), 1469 (2000)
- J. Nygren, J. Engström, J. Walewski, C. Kaminski, M. Aldén, *Meas. Sci. Technol.* **12**, 1294 (2001)
- P. Medwell, Q. Chan, P. Kalt, Z. Alwahabi, B. Dally, G. Nathan, *Appl. Opt.* **48**(6), 1237 (2009)
- R. Lucht, N. Laurendeau, D. Sweeney, *Appl. Opt.* **21**(20), 3729 (1982)
- M. Tamura, J. Luque, J. Harrington, P. Berg, G. Smith, J. Jeffries, D. Crosley, *Appl. Phys. B* **66**(4), 503 (1998)
- J. Hult, I. Burns, C. Kaminski, *Proc. Combust. Inst.* **30**(1), 1535 (2005)
- I. Burns, N. Lamoureux, C. Kaminski, J. Hult, P. Desgroux, *Appl. Phys. B* **93**, 907 (2008)
- J. Engstrom, *Development of a 2D Temperature Measurement Technique for Combustion Diagnostics Using 2-line Atomic Fluorescence*. Ph.D. thesis, Lund University (2001)
- Q. Chan, P. Medwell, P. Kalt, Z. Alwahabi, B. Dally, G. Nathan, *Appl. Opt.* **49**(8), 1257 (2010)
- P. Medwell, Q. Chan, B. Dally, Z. Alwahabi, S. Mahmoud, G. Metha, G. Nathan, *Appl. Phys. B* **107**, 665 (2012)
- Q. Chan, P. Medwell, Z. Alwahabi, B. Dally, G. Nathan, *Appl. Phys. B* **104**, 189 (2011)
- G. Zizak, J. Bradshaw, J. Winefordner, *Appl. Opt.* **19**(21), 3631 (1980)
- L.C. Allen, J.H. Eberly, *Optical Resonance and Two-Level Atoms* (Dover Publications, New York, 1975)
- R. Loudon, *The Quantum Theory of Light* (OUP, Oxford, 2000)
- J.D. Lambert, *Vibrational and Rotational Relaxation in Gases* (Clarendon Press, Oxford, 1977)
- A.E. Siegman, *Lasers* (University Science Books, Mill Valley, 1986)
- J. Dec, J. Keller, in *Symposium (International) on Combustion*, vol. 21 (Elsevier, 1988), pp. 1737–1745
- C.A. Schneider, W.S. Rasband, K.W. Eliceiri, *Nat. Methods* **9**(7), 671 (2012)
- C.K. Law, *Combustion Physics* (CUP, Cambridge, 2006)
- W. Balfour, *Mol. Phys.* **89**(1), 13 (1996)
- A. Kramida, Y. Ralchenko, J. Reader, NIST ASD Team. in *NIST Atomic Spectra Database (version 5.1)*, (2013). <http://physics.nist.gov/asd>